IEEE Access
Multidisciplinary ⋮ Rapid Review ⋮ Open Access Journal

Received 5 May 2024, accepted 19 May 2024, date of publication 27 May 2024, date of current version 3 June 2024.

Digital Object Identifier 10.1109/ACCESS.2024.3405808

RESEARCH ARTICLE

Coupled Inductor Based Boost Microinverter With Dual Mode Time Sharing Operation for Renewable Energy Applications

FAHAD M. ALHUWAISHEL, (Member, IEEE), AND NABIL A. AHMED, (Senior Member, IEEE)
Department of Electrical Engineering, College of Technological Studies, The Public Authority for Applied Education and Training, Shuwaikh, Dasman 70654, Kuwait

Corresponding author: Fahad M. Alhuwaishel (fm.alhuwaishel@paaet.edu.kw)

This work was supported in part by the Public Authority for Applied Education and Training (PAAET), and in part by the College of Technological Studies under Project TS-22-02.

ABSTRACT Household power conversion stages process significant amounts of power when they add up to form a microgrid. Microinverters are considered one of the best choices to utilize the renewable energy harvested power. Microinverter integration encounters several challenges when interfaced with expanding microgrids. This paper proposes a coupled inductor-based boost microinverter operating in dual mode time sharing technique for renewable energy applications. It is composed of an absolute sinewave modulated voltage boost converter and series capacitor connected to the secondary winding of the coupled inductor followed by a single-phase Full bridge inverter. The coupled inductor integration allows a significant reduction in current ripple and improved energy conversion efficiency. In the proposed microinverter, the DC link voltage is not required to be constant, instead, it process an absolute sinewave modulated voltage and then it is unfolded to AC and fed into the grid. The DC link capacitor is substituted by an efficient AC thin film type capacitor. The dual mode time-sharing principle intends to reduce the switching losses of the microinverter and consequently achieves high conversion efficiency. The proposed converter's analysis, design, and simulation are validated on a 2.0 kW setup system using PSIM simulation software. The feasibility and performance of this new microinverter topology is proved experimentally via laboratory prototype. The current ripple can be reduced to one half in case of matching coupled inductor primary and secondary windings compared to the typical boost converter. In another scenario, the current ripple can be fully eliminated in either of the coupled inductor windings when winding inductance equals to the mutual inductance. The proposed microinverter topology offers a notable enhancement in power conversion performance that reached 97%. In addition, a high-quality sinusoidal output current waveform of 1.1% total harmonic distortion is achieved.

INDEX TERMS Microinverter, dual mode, time-sharing, coupled-inductor, boost converter, renewable energy.

I. INTRODUCTION

Power systems around the world that aim to reduce greenhouse gas emissions are using more renewable energy sources (RES) as these sources play an important role in a sustainable energy future. However, with the integration of high share of RES generation, major challenges may arise for the secure and stable operation of the power grid [1], [2]. Therefore, power inverters play a crucial role in mitigating these challenges.

Due to their superior production, unrivaled intelligence, easy installation, small size, and adaptability, microinverters provide the most modern inverter technology available on the market [3], [4], [5], [6]. Microinverters have gained

The associate editor coordinating the review of this manuscript and approving it for publication was Inam Nutkani.

popularity, especially in residential solar installations, due to their advantages in individual panel optimization, monitoring capabilities, and enhanced safety features. Microinverters operate on a per-panel basis, allowing each solar panel to perform at its maximum potential. This contrasts with string inverters, where the performance of the entire string is limited by the output of the weakest panel. Consequently, the market for microinverters was valued more than 2.5 billion in 2020 and is projected to grow 6.5 billion by 2025 [7].

The variety of topologies suggested in literatures [8], [9], [10], [11], [12], and [13] for galvanically isolated microinverters is represented in Fig. 1(a). In order to accomplish the boost function, it primarily comprises of a DC/DC converter stage with a high frequency transformer buffer. A DC link buffer interfaced with an inversion stage converts the DC input to a high-quality 240V/50Hz AC output after the DC/DC conversion stage. On the other hand, the high frequency transformer buffer increases the system's volume and power losses. Since transformer-based inverters are said to have a peak efficiency of about 94% [14], [15], [16], [17], the researchers were motivated to find a different strategy. To supplement their current lineup of transformer-type inverters for installation in the US, several microinverter manufacturers have devised and constructed transformer less inverters. In Europe, transformer less inverters have been widely used for a while. They weight far less, do not experience the same energy losses, and therefore cost less than the bulkier same-wattage transformer-style inverters. With transformer less inverters, there are a few considerations that need to be taking care of. Both the German standard VDE 0126-1-1 and Section 690.35 of the 2014 National Electrical Code (NEC) USA standards contain specifics about these requirements [18], [19]. The family of transformer-less topologies depicted in Fig. 1(b) has been extensively studied in the literature to allow for greater efficiency and lower volumetric size of the microinverters [20], [21], [22], [23]. The non-isolated single stage without DC link buffer is shown in Fig. 1(c).

When wide band gab devices are integrated with transformer less inverters, it has been reported that power losses can be significantly reduced, setting a new efficiency record of 99% in residential applications [20]. Transformer less microinverters were successfully introduced in European and Australian markets, which led to their huge appeal in the United States. Microinverters are mostly used in low voltage single source photovoltaic and fuel cell (FC) applications. The fuel cell can be regarded as a clean energy source since it produces heat, power, and water through an electrochemical reaction using only pure hydrogen. Due to its exceptional efficiency, zero or minimal pollutant emissions, and fuel flexibility, fuel cells (FCs) are a highly sought-after alternative for power generation in the future. As a clean energy source, fuel cells have recently attracted increasing attention. Fuel cells are electrochemical devices that directly and continuously transform chemical energy from a reaction between

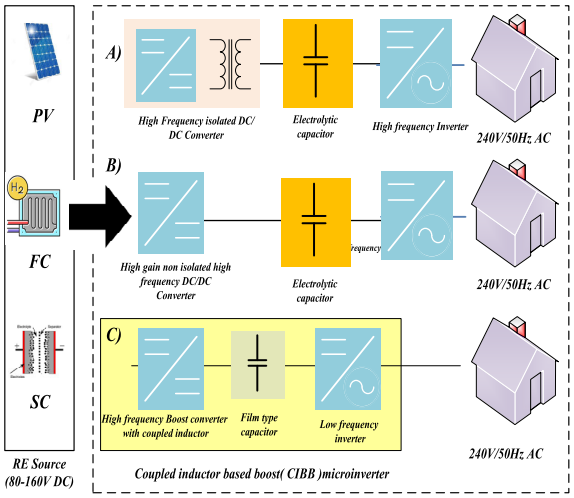

FIGURE 1. Evolution of single stage microinverters: (a) isolated two-stage, (b) non-isolated two-stage, (c) non-isolated single-stage.

an oxidant, oxygen, and a fuel, hydrogen, into electrical energy. FC systems provide a clean substitute since they are direct single stage energy conversion devices that contribute to high electrical energy conversion efficiency. One of the most promising technologies to be employed as power supply sources in various portable applications in the near future are fuel cell systems, which provide a clean alternative to energy production [24], [25], [26], [27], [28].

Due to the extremely high voltage conversion ratio, two-stage conversion is typically necessary for microinverter [31]. The DC-DC stage raises the voltage from the PV module to a higher level for grid voltage, as seen in Fig. 2. By using pulse width modulation (PWM), the DC/AC stage transforms the DC voltage into the AC line voltage. As seen in Fig. 2(a), the high capacitance across the DC connection allows for stable voltage, which acts as an energy buffer during the conversion of DC energy into AC energy. A significant factor to consider with microinverters is the need for a compact size passive power decoupling (PPD) DC link capacitor. The single-phase inverter's second harmonic power ripple is handled via the DC link. Moreover, the DC connection design is complicated due to the need to accommodate the strict specification of a 1% DC bus voltage ripple [25]. Because the electrolytic capacitor has the highest permittivity and energy density, it is the only option available for DC link capacitor selection. Unfortunately, electrolytic capacitors have limited RMS current capability, a short lifespan, a high ESR, a high ESL, and a loss of capacitance. To process the second harmonic power, several active power decoupling techniques have been presented in the literature; however, these additional decoupling techniques demand more space and dimensions.

To keep the DC link voltage constant, the design shown in Fig. 2(b) does not utilize a high capacitance at the DC link [32]. It permits fluctuations in accordance with the grid voltage's double line frequency. In the subsequent step, the DC current is unfolded to AC and fed into the grid in the

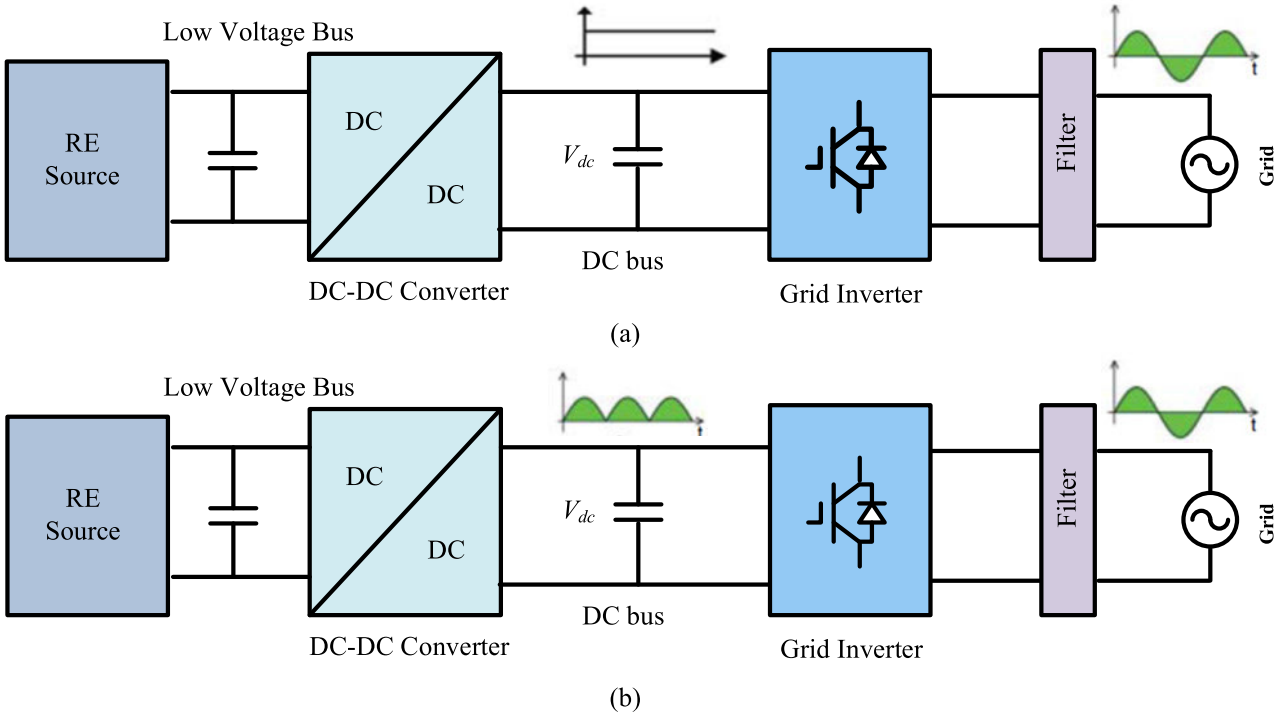

FIGURE 2. Types of microinverters: (a) DC link for steady voltage (b) Current-unfolding approach.

second stage. At the DC/AC conversion step, the unfolding technique intends to reduce the high frequency switching loss. Double-line frequency voltage ripples can only be reduced by large capacitance at the input link because most microinverters are intended to be linked to a single-phase AC grid. Nonetheless, industry experience has demonstrated that this architecture may reach above 96% efficiency, which is substantial for the high gain voltage conversion ratio [31].

The concept of unfolding stage is modified and extended to widely utilized dual-mode time-sharing inverters [32], [33], [34], [35], [36]. Time sharing operations have been investigated as a potential small film type capacitor replacement for large dc-link capacitors [32]. Both the inverter and the DC-DC converter stages are permitted to switch for a portion of the entire duration when operating in a time-sharing capacity. For microinverters, on the other hand, when low voltage and high current application are necessary, time-sharing approaches are not investigated. In [8], a selective dual-mode time-sharing sinewave absolute value modulated boost converter with bypass diode is presented and the DC-link capacitor is effectively replaced by a thin film AC capacitor. Figs. 3 and 4 illustrate a comparison of circuit configuration and operation principles of two-stage and dual mode time sharing inverters with bypass diode. In Fig. 3, the boost DC-DC converter and the FB single-phase inverter make up the conventional two-stage microinverter. To boost the low and uncontrolled DC voltage of the renewable energy systems to a constant output voltage (300-400 V), the boost switch S_b in the first power processing stage is

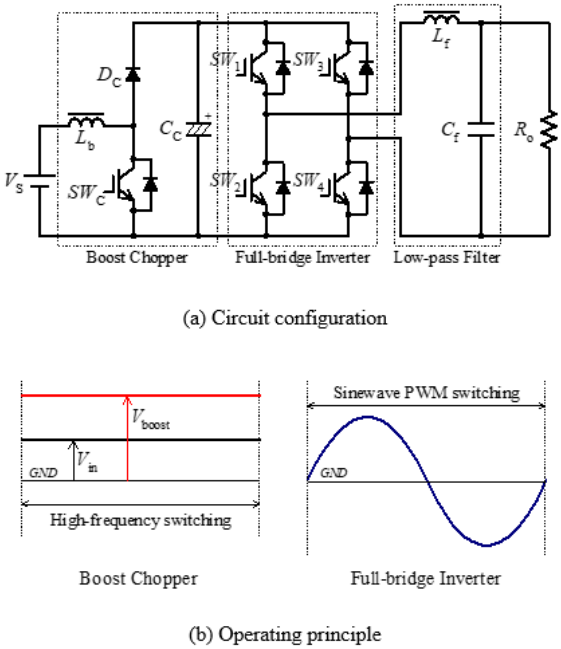

FIGURE 3. Conventional two-stage microinverter.

utilized and always operated at high switching frequency. Similarly, the FB inverter switches ($S_1 - S_4$) in the second processing stage are always switching at PWM high switching frequency. High switching frequency operation of both stages leads to high switching losses and consequently low

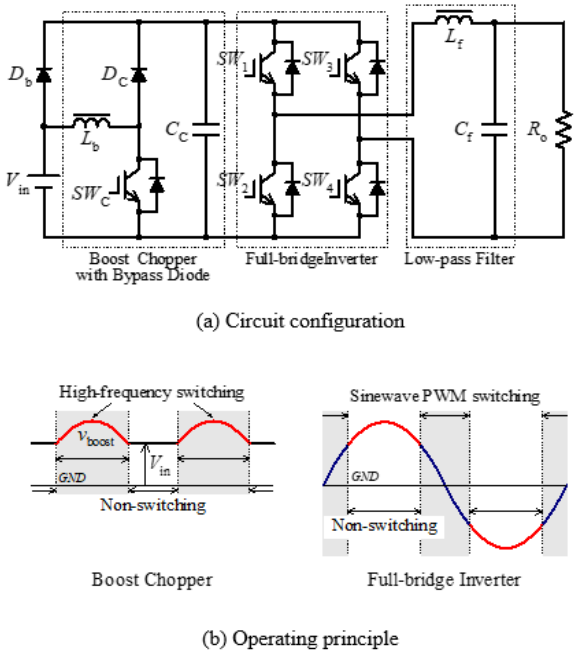

FIGURE 4. Conventional Time sharing microinverter.

power conversion efficiency. In addition, to maintain steady DC link voltage, the boost converter side requires a huge, heavy unreliable electrolytic capacitor. With the drawbacks of electrolytic capacitors as limited lifetime, large leakage currents, value tolerances and equivalent series resistance, lighter microinverter are unachievable.

Fig. 4 illustrates a dual-mode time-sharing PWM inverter with a bypass diode. It can achieve high conversion efficiency compared to the two-stage converter for a wide range of output power. The DC-DC boost converter is not required to maintain a steady output voltage at the DC link; it modulates the DC-link voltage to a quasi-sinewave ac absolute value. As a result, it is possible to drastically lower the DC-link capacitor or to replace it with a small size ac capacitor. However, this topology encounters a relatively high inductor ripple current which constrains the inductor sizing for continuous mode operation, especially at low input voltage. In addition, this large inductor design reduces the power conversion efficiency especially at high power ratings. Furthermore, the inductor current ripple is crucial agent for renewable energy application such as fuel cell and PV where high source ripple current significantly degrades the RE source lifetime. A possible remedy to these drawbacks is deploying coupled inductor-based converters. Coupled inductor converters offer benefits such as reduced size and weight compared to traditional single-inductor converters [37]. They also provide improved performance in terms of efficiency, voltage regulation, and electromagnetic interference (EMI) due to their inherent magnetic coupling. In this paper, a single stage transformer less coupled inductor microinverter with time-sharing operation is proposed as a solution to these knowledge gaps.

II. PROPOSED COUPLED INDUCTOR-BASED BOOST MICROINVERTER

Fig. 5 illustrates the proposed coupled inductor-based boost (CIBB) microinverter which is mainly composed of coupled inductor based absolute sinewave modulated voltage boost converter followed by a single-phase FB inverter with an LC filter. A series capacitor Cs is connected to the secondary winding of the coupled inductor to reduce the inductor ripple current. The proposed microinverter features efficient dual-mode timesharing operation between the boost converter and the FB inverter. As a result, low switching frequency is the FB inverter's primary operating frequency. High switching frequency is only used to switch a small portion of the line frequency, when the input voltage is greater than the absolute sinewave modulated voltage. In the proposed topology, the dc link capacitor is substituted by an efficient AC thin film type capacitor. Due to the substantial reduction of the DC-link and the removal of the isolation transformer, the boost conversion and the FB inverter inversion stages are combined into a single stage. The following benefits of the suggested time-sharing microinverter topology are:

1. The large-lossy electrolytic DC link capacitor is eliminated in the suggested topology and is replaced with an embedded, small-sized film-type capacitor.
2. The proposed microinverter has a high-power conversion efficiency when it operates in the time-sharing mode.
3. Fit for applications requiring high current and low input voltage as fuel cell systems.
4. The inverter only uses a small-time interval of the line frequency to operate in high switching PWM.
5. A sinusoidal output voltage of superior quality.
6. The coupled inductor features reduced current ripple.

The operation principles and the dual mode time-sharing working depicted in Fig. 5 are similar to that given in [32] and [35]. In which, the boost switch (S_b) and inverter switches ($S_1 - S_4$) do not require to operate at high switching frequency at the same time as in the two-stage inverter. When the input dc voltage is less than the absolute value of the required sinusoidal instantaneous output voltage, the boost converter, which is a current-fed circuit, operates in a high switching frequency PWM operation mode to boost the input voltage and produce a quasi-sinusoidal pulse modulated voltage waveform at the intermediate dc bus. The switches (S1 through S4) in the FB inverter are either in a line frequency switching operation or at PWM operation mode when the input dc voltage is greater than the absolute value of the required sinusoidal instantaneous output voltage around zero voltage crossing. The controller diagram of the proposed CIBB microinverter is shown in Fig. 6. The upper portion of the diagram is responsible of controlling the boost dc-dc unit via generating suitable gating signals sent to S_b to obtain a quasi-absolute sinusoidal modulated voltage at the intermediate bus. The duty cycle of the boost switch S_b during the boost operation mode is identical to the standard boost converter. The lower portion expresses the control of the FB

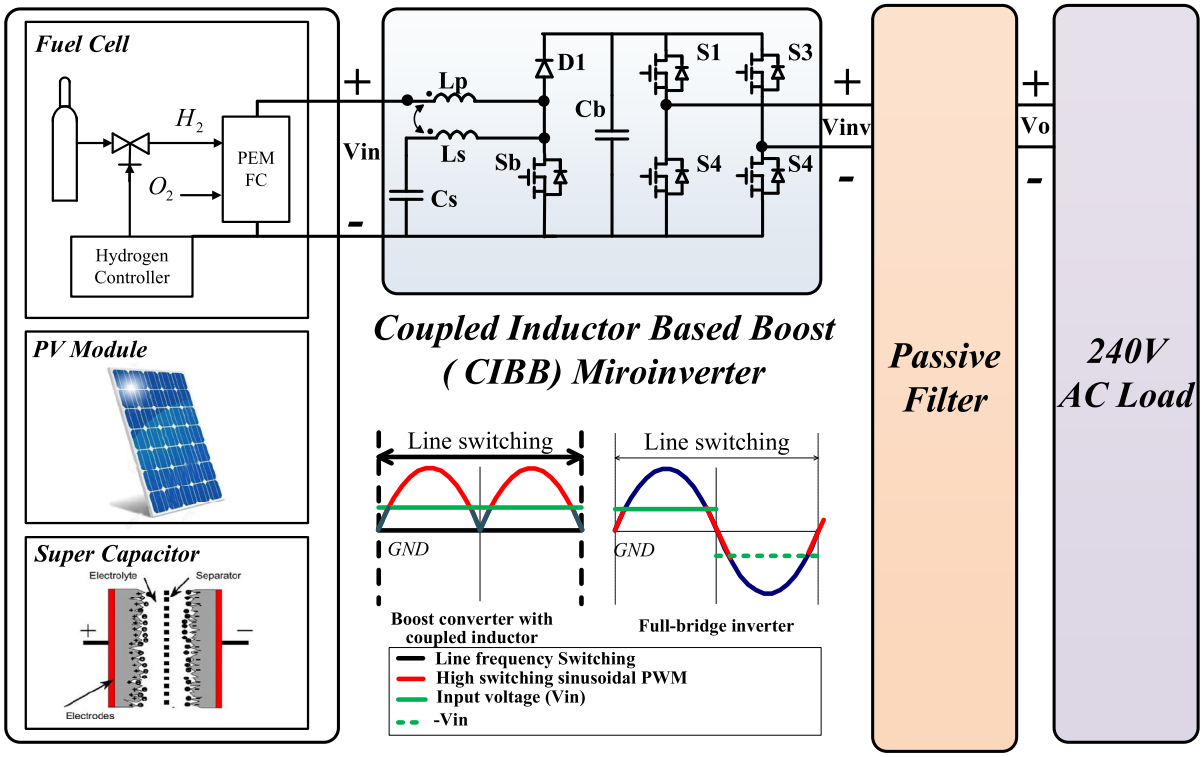

FIGURE 5. Proposed coupled inductor-based boost microinverter operating.

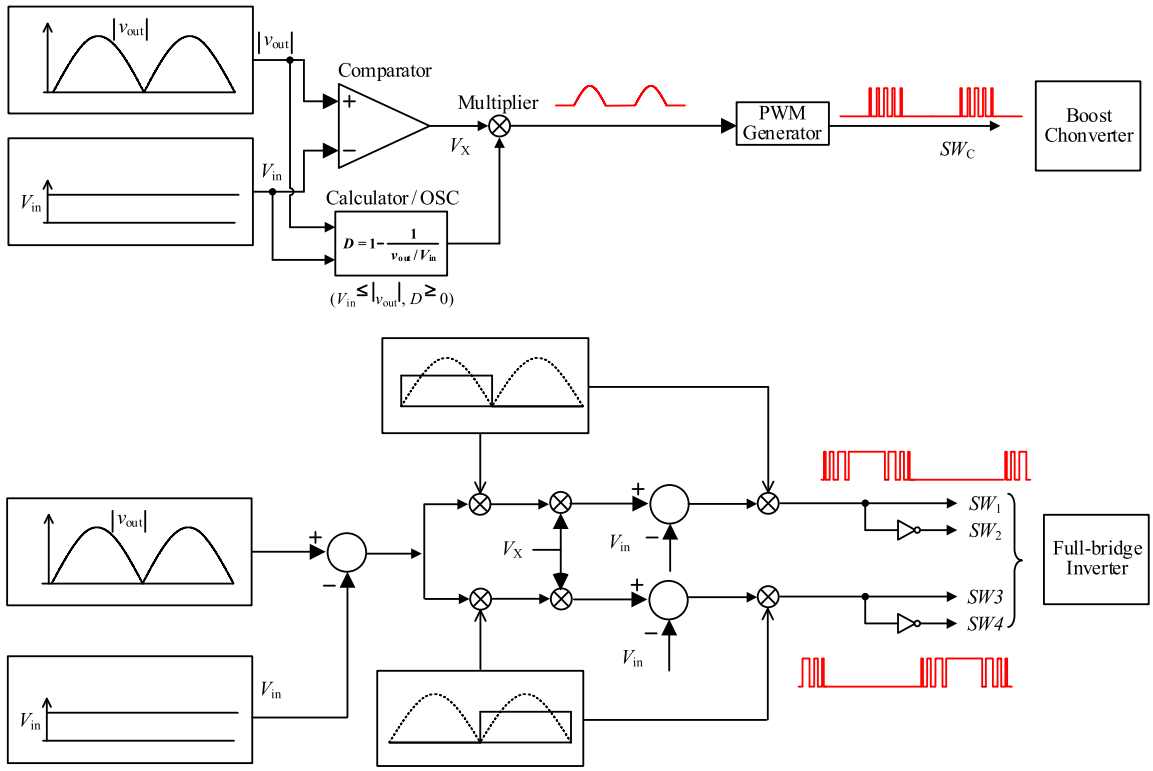

FIGURE 6. Schematic diagram of the control circuit.

inverter. The FB inverter operates as unfolding inverter when the input voltage is less than the absolute value of the output voltage $|v_o(t)|$. When V_{in} is more than more than $|v_o(t)|$, the FB inverter operates in sinusoidal PWM switching scheme.

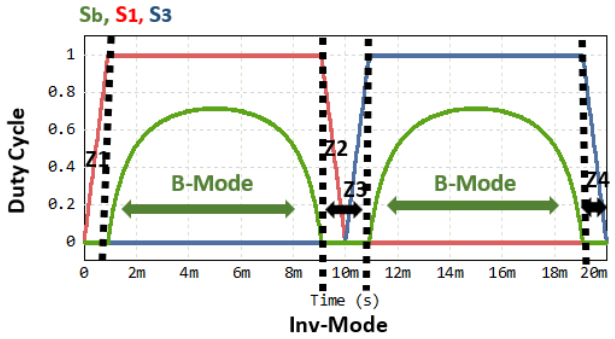

FIGURE 7. Boost and inverter operation modes of the proposed CIBB microinverter.

One of the main advantages of the proposed topology is that it does not apply high capacitance at the intermediate bus to maintain the steady DC-link voltage since the intermediate bus voltage exhibits an ac voltage instead of a DC voltage. It is an absolute quasi-sinewave modulated voltage that occurs in the intermediate bus. It permits voltage fluctuations in accordance with the grid voltage's double line frequency. In the subsequent step, this voltage is unfolded to AC and fed into the grid. The unfolding approach intends to reduce the high frequency switching loss at the DC/AC conversion. As a result, a more efficient, reliable and compact AC film capacitor is employed as a replacement for bulky, and lossy electrolytic DC link capacitor. The detailed CIBB operation will be analyzed in the following section.

III. ANALYSIS AND PRINCIPLE OF OPERATION

The Schematic diagram of the control circuit of the proposed CIBB microinverter is shown in Fig. 6. The input can be any type of renewable energy sources (RES) such as fuel cell (FC), PV or super capacitor (SC). The input voltage of the RES is assumed to be in the range of 80-160. The operation of the proposed CIBB microinverter is detailed in Figs. 7-9 and will be explored in this section. The proposed CIBB microinverter can operate in two operation modes; boost mode (B-mode) and inverter mode (Inv-mode) as illustrated in Fig. 7. In boost mode the major switches responsible of shaping the output sinewave is boost switch S_b and D_1. The duty cycle of S_b is controlled to follow absolute value modulated sine wave of the desired output voltage as illustrated in Fig. 7. In this mode, only one active switch is operated via a high switching frequency scheme. The following FB inverter operated at line frequency power efficient switching scheme. The FB inverter is only used to reverse intermediate modulated voltage V_{cb} during the negative half cycle to obtain the desired sinusoidal output voltage. This mode occurs when the input voltage is lower than the absolute value of the output voltage. On the other hand, during the inverter mode, the FB inverter is fully responsible for shaping the output sinusoidal waveform as demonstrated in Fig. 6, and this happens when the input voltage is greater than the absolute value of the output voltage. This mode duration is kept being minimal since that it involves the FB switches ($S_1 - S_4$) operating at high switching frequency. The inverter-mode operates in four intervals of Z_1 to Z_4 as displayed in Fig. 7. The operation switching states for boost-mode and inverter-mode are detailed in this section.

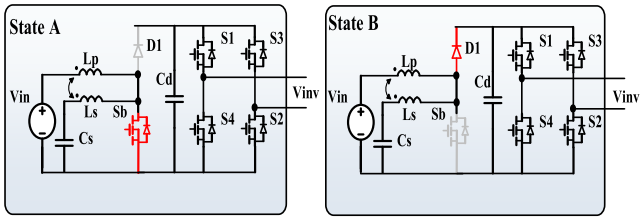

FIGURE 8. Operation states of the proposed CIBB microinverter during the boost-mode.

A. BOOST MODE OPERATION

Boost-operation mode is activated when V_{in} is less than the V_o during the positive half cycle of the output voltage V_o. The boost mode is similarly activated when V_{in} is less than $|V_o|$ as demonstrated in Fig. 8. In this operation mode, the boost converter unit depicted in Fig. 8 is responsible to process the whole input power with only one active switch operates in high switching frequency scheme as shown in red color while, the FB inverter switches operate at line frequency. Compared to the traditional boost converter shown in Fig. 3, this approach features a coupled inductor. The secondary winding of the coupled inductor is connected in series with a capacitor. It is feasible to design the turn's ratio, inductance value, coupling coefficient (K), and switch's turning on time in order to produce various output voltage levels. The power switch S_b and the diode D_1 in the boost-mode create the main pathway of the current towards the intermediate bus capacitor. S_b is controlled to create a portion of an absolute sine wave as shown in Fig. 8. Two diagonal switches $S_1 - S_2$ or $S_3 - S_4$ of the following FB inverter, in turns, are turned ON to produce to construct a portion of the output sinusoidal voltage as:

$$v_o = V_m \sin(wt) \tag{1}$$

The duty cycle of the boost switch S_b during the boost operation mode can be found as

$$d(t) = \frac{|v_o(t)| - V_{in}}{|v_o(t)|} \tag{2}$$

This mode of operation is divided into two operation states as detailed below:

1) STATE A WITH $0 \leq t < t_1$

During this state the boost switch S_b is turned ON and both the coupled inductor windings (L_p and L_s) are charged, thus, the energy is stored in coupled inductor. Therefore, the primary winding current of the coupled inductor is increased from its minimum value to its maximum value with a change of Δi_{LP} in the steady state. Consequently, the induced voltage in the secondary winding of the coupled inductor will be positive and responsible of charging the capacitor C_s. In state A, the

stored energy in the intermediate bus capacitor C_b is transmitted to the load via the FB inverter. The coupled inductor primary and secondary windings voltages (V_{LP} and V_{LS}) can be expresses as:

$$V_{LP} = L_P \frac{di_{L_p}}{dt} + M \frac{di_{L_s}}{dt} = V_{in} \tag{3}$$

$$V_{LS} = L_s \frac{di_{L_s}}{dt} + M \frac{di_{L_p}}{dt} = V_c \tag{4}$$

The voltage across the capacitor C_s is found as:

$$V_{c1} = V_{in} \tag{5}$$

The mutual inductance (M) is known as:

$$M = K\sqrt{L_P L_S} \tag{6}$$

where K is the coupled inductor coefficient. Therefore, the ripple current of the primary winding (Δi_{LP}) and secondary winding Δi_{LS} is equated as follows:

$$\Delta i_{LP} = \frac{V_{in} - K\sqrt{L_P L_S}\frac{di_{L_s}}{dt} t_1}{L_P} \tag{7}$$

$$\Delta i_{LS} = \frac{V_{in} - K\sqrt{L_P L_S}\frac{di_{L_P}}{dt} t_1}{L_S} \tag{8}$$

2) STATE B WITH $t_1 \leq t < t_2$

In state B, S_b power switch is turned OFF while diode D_1 is turned ON as shown in Fig. 8. The primary winding voltage V_{LP} reverse its polarity and the primary winding current starts to decrease. Furthermore, this negative voltage value is induced in the secondary winding, which results in a drop in secondary winding current equals to the current flowing through the series capacitor C_s. The coupled inductor primary and secondary windings voltages (V_{LP} and V_{LS}) are found to be:

$$V_{LP} = L_P \frac{di_{L_p}}{dt} + M \frac{di_{L_s}}{dt} = V_{in} - V_{cb} \tag{9}$$

$$V_{LS} = L_s \frac{di_{L_s}}{dt} + M \frac{di_{L_p}}{dt} = V_{c1} - V_{cb} \tag{10}$$

The, the following relation is concluded:

$$V_{c1} - V_{cb} = V_{in} - V_{cb} \tag{11}$$

The coupled inductor current reaches its minimum value at the end of this operation state at the moment of t2 when the switch S_b is again turned ON at beginning of the next switching cycle. The current ripples of the primary and secondary winding are obtained as:

$$\Delta i_{LP} = \frac{-V_{in} + V_{cb} - K\sqrt{L_P L_S}\frac{di_{L_s}}{dt}(t_2 - t_1)}{L_P} \tag{12}$$

$$\Delta i_{LS} = \frac{-V_{in} + V_{cb} - K\sqrt{L_P L_S}\frac{di_{L_P}}{dt}(t_2 - t_1)}{L_S} \tag{13}$$

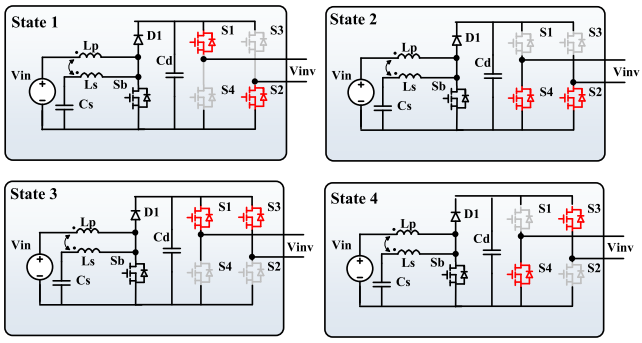

FIGURE 9. Operation states of the proposed CIBB microinverter during the inverter-mode.

B. INVERTER OPERATION MODE

The inverter-mode operation is used when V_{in} is more than V_o during the positive half cycle of the output voltage V_o. This mode is also used when V_{in} is more than $|v_o(t)|$ during the negative half cycle of the output voltage V_o. The inverter-mode of operation can be divided into four operating intervals, Z1-Z4 as shown in Fig. 6. In Z1 and Z2, S_1 and S_4 switches at high switching frequency unipolar sinusoidal PWM modulation as depicted in Fig. 9. In Z1, the duty cycle reference of S_1 goes gradually from 0 to 1. Inversely, S_4 gradually is reduced from 1 to 0. Throughout Z2, the duty cycle reference of S_1 gradually reduced from 1 to 0 while S_4 gradually increased from 0 to 1. Meanwhile, S_2 stays ON while S_3 stays OFF during Z1 and Z2 zones. As a result, States 1 and 2 are obtained during Z1 and Z2 where:

$$\begin{cases} +V_{in}, S_1, \& S_2 \text{ are ON} \\ 0, S_2, \& S_4 \text{ are ON} \end{cases} \tag{14}$$

Similarly, Z3 and Z4 are formed to fully construct the output sinusoidal sinewave as illustrated in Fig. 9. Thus, switches S_2 and S_3 operates at high switching frequency unipolar sinusoidal PWM modulation. In Z3, the duty cycle reference of S_3 goes gradually from 0 to 1 and S_2 is reduced from 1 to 0. Considering Z2, the duty cycle reference of S_3 is gradually increased from 0 to 1 while S_2 is gradually decreased from 1 to 0. Meanwhile, S_4 stays ON while S_1 maintains OFF condition during both Z1 and Z2 zones. As a result, States 3 and 4 are attained during Z1 and Z2 where:

$$\begin{cases} -V_{in}, S_3, \& S_4 \text{ are ON} \\ 0, S_3, \& S_1 \text{ are ON} \end{cases} \tag{15}$$

C. COUPLED INDUCTOR CURRENT RIPPLE REDUCTION

The proposed topology can reduce the ripple of input current when compared with conventional boost converter which will be discussed in detail in the following. Starting with combining equations (3) and (4) during state A of the boost mode, leads to:

$$V_{in} = L_P \frac{di_{L_p}}{dt} + M \frac{di_{L_s}}{dt} = M \frac{di_{L_p}}{dt} + L_s \frac{di_{L_s}}{dt} \tag{16}$$

Equation (16) can be solved using Cramer's rule to obtain the coupled inductor current ripples $\frac{di_{L_p}}{dt}$ and $\frac{di_{L_s}}{dt}$ as follows:

$$\Delta = \begin{vmatrix} L_p & M \\ M & L_s \end{vmatrix} = L_p L_s - M^2 \tag{17}$$

$$\frac{di_{L_p}}{dt} = \frac{V_{in}\,(L_S - M)}{L_P L_S - M^2} \tag{18}$$

$$\frac{di_{L_s}}{dt} = \frac{V_{in}\,(L_P - M)}{L_P L_S - M^2} \tag{19}$$

From Equation (18) and (19), it's clear to note that the relation between the coupled inductor parameters plays an important role for the magnitude of the ripple currents. Thus, the condition for L_P current ripple elimination

$$L_S = M \tag{20}$$

Similarly, the condition for L_S current ripple elimination is

$$L_P = M \tag{21}$$

Averaging equations (18) and (19) and assuming ideal components, the coupled inductor windings current ripples can be simplified as:

$$\Delta i_{L_p} = \frac{DV_{in}\,(L_S - M)}{(L_P L_S - M^2) f} \tag{22}$$

$$\Delta i_{L_s} = \frac{DV_{in}\,(L_P - M)}{(L_P L_S - M^2) f} \tag{23}$$

The minimum primary winding inductance L_{pmin} to maintain continues conduction mode can be computed as follows:

$$L_{pmin} = \frac{R\,(1-D)^2 \cdot D\,(L_S - M)}{2fL_s} + \frac{M^2}{L_s} \tag{24}$$

Considering conventional ideal boost converter operating in continues conduction mode, the boost inductor current ripple Δi_{L_B} is known as:

$$\Delta i_B = \frac{DV_{in}}{L_B f} \tag{25}$$

A figure of merit λ_1 describing a ripple reduction factor in coupled inductor primary winding current ripple Δi_{L_S} compared to the conventional boost converter is defined as:

$$\lambda_1 = \frac{\Delta i_{L_p}}{\Delta i_B} = \frac{L_B\left(L_S - K\sqrt{L_P L_S}\right)}{L_P L_S\left(1 - K^2\right)} \tag{26}$$

Similarly, a figure of merit λ_2 describing ripple reduction factor of the coupled inductor secondary winding current is introduced as:

$$\lambda_2 = \frac{\Delta i_{L_s}}{\Delta i_B} = \frac{L_B\left(L_P - K\sqrt{L_P L_S}\right)}{L_P L_S\left(1 - K^2\right)} \tag{27}$$

Therefore, when λ_1 and λ_2 is less than one, a lesser current ripple is resulted leading to lower inductor size requirement. Consequently, this will reflect an advantageous status leading to lesser power losses situation.

Fig. 10 shows the relation between the values of the ripple factors λ_1 and λ_2 for matched coupled inductor parameters of

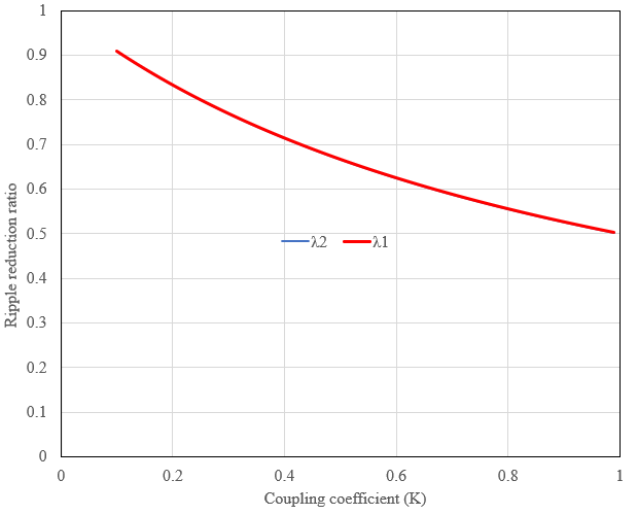

FIGURE 10. Ripple reduction factor in case of matched L_p and L_s.

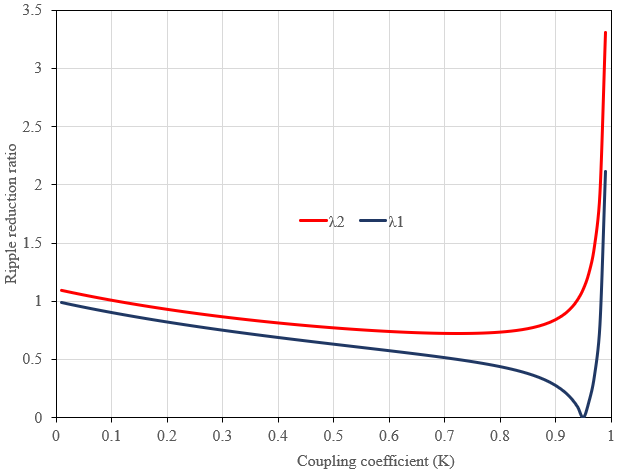

FIGURE 11. Ripple reduction factor in case of unmatched L_p and L_s.

$L_p = L_s = 150\mu$H at different coupling coefficients K. It can be observed that the inductor current ripple is strongly dependent on the coupling coefficient K of the coupled inductor. In order to have the maximum inductor current ripple reduction, the coupled inductor should have high K and also have enough leakage inductance to reduce output current ripple, simultaneously. The same relation for unmatched coupled inductor parameters $L_p = 150\,\mu$H and $L_s = 135\mu$H is depicted in Fig. 11. From Fig. 10, it can be observed that the ripple factors λ_1 and λ_2 are equal and inversely proportional to the coupling coefficients. In Fig. 11, the ripple factors λ_1 and λ_2 are unequal and they are decreasing with the coupling coefficient to some value (0.95) after that they start to increase again. At a K=0.95, the coupled inductor parameters $L_p = 150\,\mu$H and $L_s = 135\mu$H satisfy equation (20), therefore the ripple factors λ_1 approaches zero while λ_2 ha as a significant value.

Figs. 10 and 11 demonstrate that the coupled inductor is characterized with reduced current ripple when compared with typical single winding inductor. This reduced current

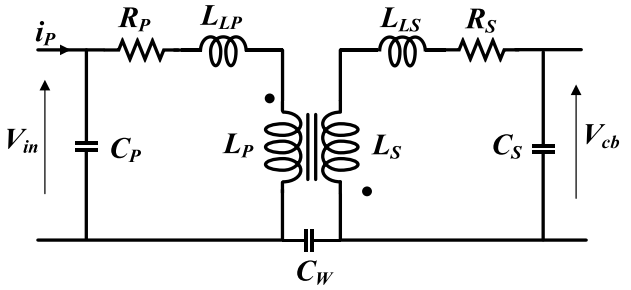

FIGURE 12. Circuit model of coupled inductor with additional parasitic elements.

in ripple requires a suitable design of coupled inductor as demonstrated in equations (20)-(24) to improve the inductance power density. As a result, smaller core, shorter winding and less cooling etc,. and eventually lesser power losses with high conversion efficiency are achieved at the same power rating. In [38], its shown that the integration of coupled inductor features higher power efficiency as well as higher gain confirming with these findings. It can be observed that the inductor current ripple is strongly dependent on the coupling coefficient K of the coupled inductor. In order to have the maximum inductor current ripple reduction, the coupled inductor should have high coupling coefficient K and also have enough leakage inductance to reduce output current ripple, simultaneously. As a result, coupled inductor with high coupling coefficient K and symmetrical inductances are selected for this work due to its reduced current ripple in both primary and secondary winding. To achieve such design, there are several existing coupled inductor structures that could be utilized to obtain high value of the coupled coefficient K [39], [40].

D. COUPLED INDUCTOR PARASITIC ELEMENTS IMPACTS ON CIBB MICROINVERTER

This subsection analyzes the effect of the coupled inductor parasitic elements on the CIBB microinverter performance. The circuit model of coupled inductor with additional parasitic elements is described in Fig. 12 [41], [42]. The corresponding parameters of this model are listed in Table 1.

Given the voltage gain and power efficiency as the criteria of interest, the parasitic capacitors are neglected for their insignificant effect on CIBB Microinverter performance. For a high magnetic coupling K, the leakage inductances can also be neglected. The non-ideal voltage gain and the efficiency are evaluated having in mind that parasitic resistances in the windings (copper resistance) usually produce the biggest impact on the voltage gain and efficiency, especially where multiple windings are used [43]. These calculations are conducted using small-ripple approximation, voltage-second balance, and capacitor-charge balance. By selecting coupled inductor with matched primary and secondary winding inductances, the current ripple in the secondary winding will be reduced to less than 8% of the primary winding as it will be shown in the simulation results section, as a result the effect of secondary winding branch is ignored.

TABLE 1. Simulation constants and circuit parameters.

Parameter	Symbol	Value
Primary inductance	L_P	150 µH
Primary leakage inductance	L_{LP}	1.6 µH
Primary winding capacitance	C_P	28.5 pF
Primary winding resistance	R_P	1.5 mΩ
Secondary inductance	L_S	150 µH
Secondary leakage inductance	L_{LS}	1.6 µH
Secondary winding capacitance	C_S	28.5 pF
Secondary winding Resistance	R_S	1.5 mΩ
Interwinding Capacitance	C_W	51.6 pF

Using the voltage second balance analysis, leads to the following equation:

$$\bar{v_L} = V_{in} - I_P R_P - (1 - D)\, V_{cb} = 0 \tag{28}$$

The current- charge balance principal is applied to further analyze the resulted circuit as follows:

$$\bar{i_c} = (1 - D)\, I_P - \frac{V_{cb}}{R_o} = 0 \tag{29}$$

Equations (28) and (29) are solved for V_{cb}, then the voltage gain is given as:

$$\frac{V_{cb}}{V_{in}} = \frac{1}{(1-D)(1+\frac{R_P}{R_o(1-D)^2})} \tag{30}$$

Similar to boost converter analysis, the transformer in Figure can be eliminated when referring V_{in} and R_P to the transformer secondary side. The circuit can also be solved directly for the inductor current I_{LP} as:

$$I_P = \frac{V_{in}}{R_o\,(1 - D)^2\,(1+\frac{R_P}{R_o(1-D)^2}} \tag{31}$$

Since the I_{LP} is also the input current then the resulted efficiency of the converter when only considering the approximated coupled inductor model is:

$$\eta = \frac{1}{1 + \frac{R_P}{R_o(1-D)^2}} \tag{32}$$

The output voltage gain and the conversion efficiency as a function of the duty cycle when considering the effect of the coupled inductor wining resistance is demonstrated in Figs. 13 and 14 for different values of the primary wining resistance. It can be noticed that the inductor winding resistance causes a major qualitative change in the voltage gain and the conversion efficiency, especially at high duty cycles more than 60%. Fig. 15 illustrates the relationship between the voltage gain and the conversion efficiency.

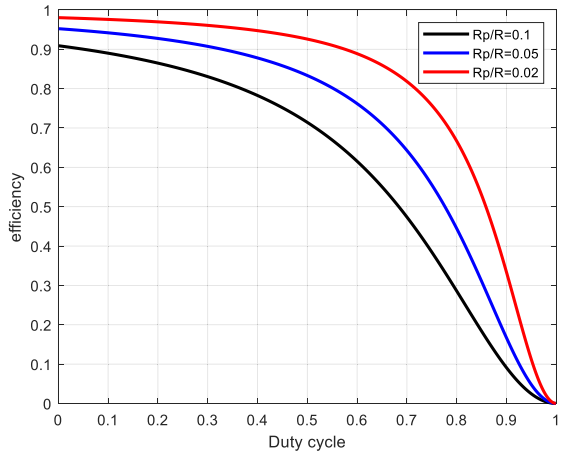

FIGURE 13. Circuit model of coupled inductor with additional parasitic elements.

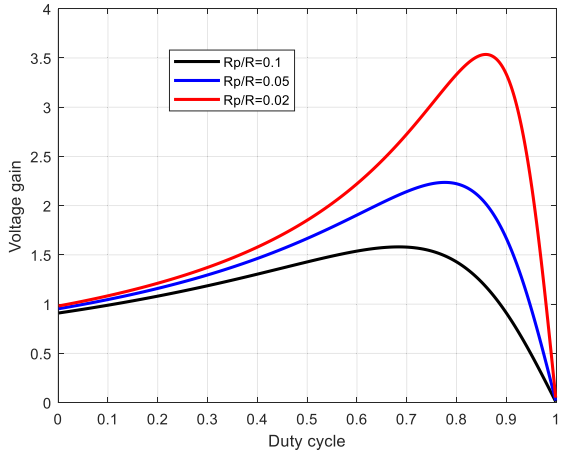

FIGURE 14. Circuit model of coupled inductor with additional parasitic elements.

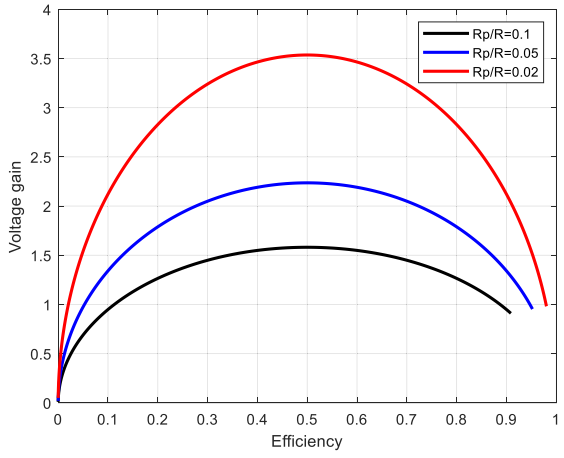

FIGURE 15. Circuit model of coupled inductor with additional parasitic elements.

IV. SIMULATION RESULTS

The proposed CIBB microinverter described in Fig. 5 is tested in PSIM software version 2021 to validate its operation principle. The simulation parameters are tabulated in Table 2.

TABLE 2. Simulation constants and circuit parameters.

Parameter	Symbol	Value
Rated power	P_o	2.0 kW
Input voltage	V_i	80 V
Output voltage	V_o	240 V
Coupled inductor	L_P	150 µH
	L_S	150 µH
	K	0.93
Series capacitor	C_s	10 µF
Intermediate capacitor	C_b	2.2 µF
Filter capacitor	C_o	10 µF
Filter Inductor	L_o	2 mH
Switching frequency	f_s	40 kHz

Fig. 16 shows the gating signal for the proposed topology generated from the control circuit shown in Fig. 6. Fig. 17 emphasized three design cases for the coupled inductor for the integrated boost DC-DC boost converter unit. Case 1 (described in red) illustrates a matching situation of coupled inductor windings of $L_p = L_s = 150\mu$H with a lower coupling coefficient of $K = 0.7$. Thus, the resulting primary winding current ripple is at its maximum while the secondary current ripple is at a relatively lower value. Case 2 (described in blue) expresses an increase in the coupling coefficient of $K = 0.93$ with matching $L_p = L_s = 150\mu$H of the coupled inductor, which slightly reduces both primary and secondary current ripples. Case 3 (described in black) demonstrates unmatching valuers of $L_p = 150\,\mu$H and $L_s = 135\mu$H that satisfies equation (21) with a coupling coefficient of $K = 0.95$. In this case, the ripple reduction ratio in the primary winding approaches zero as shown in Figs. 11 and 17. In contrary, the current ripple in the secondary winding is at its worst value compared to the other two cases. Fig. 18 is a zoomed-out version of Fig. 17 to fully view the coupled inductor currents for an extended period for the last two cases.

Fig. 19 expresses the waveforms of intermediate modulated voltage V_{cb} as well as the inverter output voltage V_{inv} before filtering as shown in Fig. 5. It can be confirmed that CIBB Microinverter is successfully operating at a dual-mode time sharing principles following the control circuit shown in Fig. 6. Fig. 20 expresses the simulated waveforms of the intermediate bus current, coupled inductor primary and secondary winding currents. A high-quality waveforms of output voltage V_o and output current I_o for a typical 2kW are illustrated in Fig. 21.

Table 3 describes the harmonic content and their percentile compared to the 50Hz fundamental frequency. The CIBB microinverter achieved a THD of 16.29% at high switching frequency of 40kHz before filtration. Therefore, a smaller LC filter could also be employed and CIBB can realize a

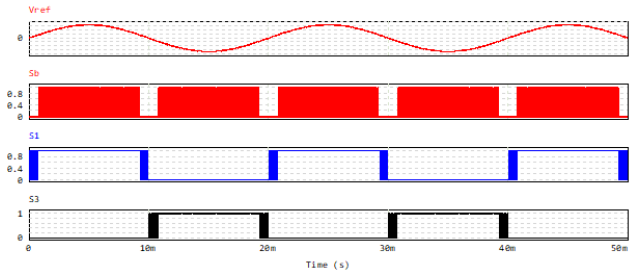

FIGURE 16. Gating signals of the proposed CIBB Micro derived from the control circuit in Fig. 6.

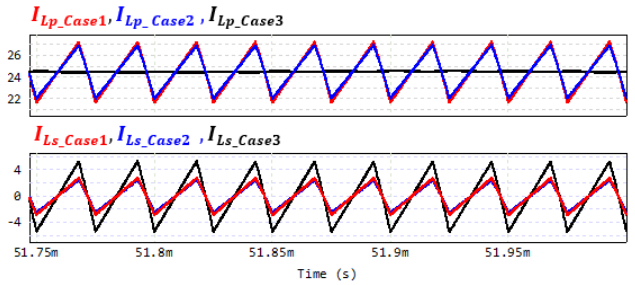

FIGURE 17. Coupled inductor design, Case 1: K= 0.7 Ls=Lp = 150μH, Case 2: K= 0.93 Ls=Lp = 150μH and Case 3: K= 0.95 Ls=135μH Lp = 150μH.

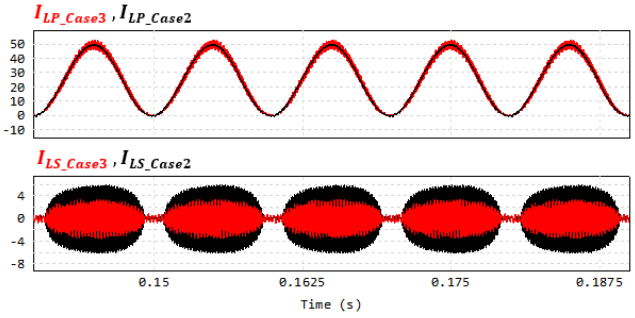

FIGURE 18. A Zoomed-out coupled inductor current waveforms for cases 2 and 3.

high grade THD. Fig. 23 describes the relevant harmonic spectra of output voltage. Fig. 24 shows the relevant harmonic spectra of output current. It can be noticed that a high-quality sinusoidal output current is realized with a total harmonic distortion of 2.5% obtained via Fast Fourier Transform (FFT) function tool provided by PSIM 2021 simulation software. This complies with the IEEE 519-2014 standards that states the voltage THD should be less than or equal 5% limit in the point of common coupling measurements [44], [45].

Fig. 25 demonstrates the power loss of the coupled inductor boost converter at 2.0 kW rated output power and 160 V input voltage and different coupling coefficients from zero coupling coefficient to a full coupling. It is clear to note that increasing the coupling coefficient leads to a decrease in the power loss of the boost converter. The total system conversion efficiency is depicted in Fig. 26, which illustrates a high total system conversion efficiency at high coupling

TABLE 3. Significant harmonic contents of unfiltered inverter voltage.

Frequency (kHz)	40	80	120	160	200	240
Amp.	13.57	7.72	5.23	3.67	2.77	2.57
%	0.04	0.023	0.02	0.011	0.008	0.007
THD	16.29%					

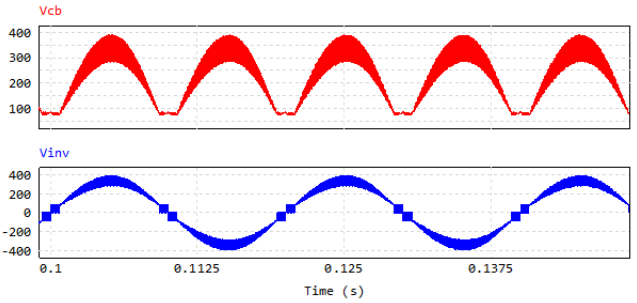

FIGURE 19. Waveforms of the intermediate modulated voltage and the resulting inverter output voltage before filtration.

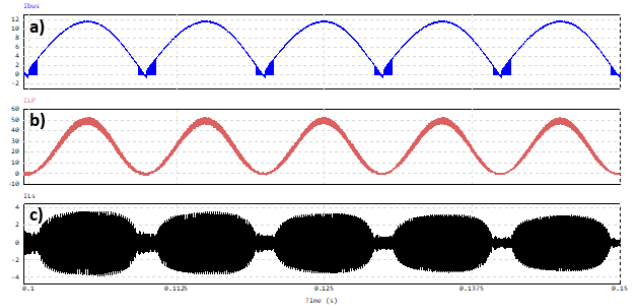

FIGURE 20. Simulation waveforms of a) Intermediate bus current, b) Primary winding current, and c) Secondary winding current.

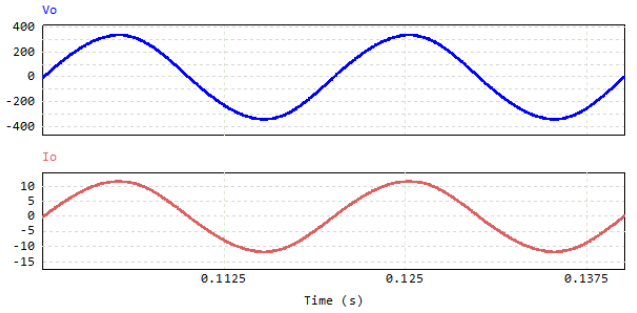

FIGURE 21. High quality AC output voltage and the output current waveforms.

coefficient due to the reduction in the power loss of the boost converter.

V. EXPERIMENTAL WORK

An experimental test was conducted on a 2.0 kW hardware setup to validate the analysis and the performance of the proposed microinverter at an input voltage of 160 V with the specifications and circuit parameters listed in Table 4.

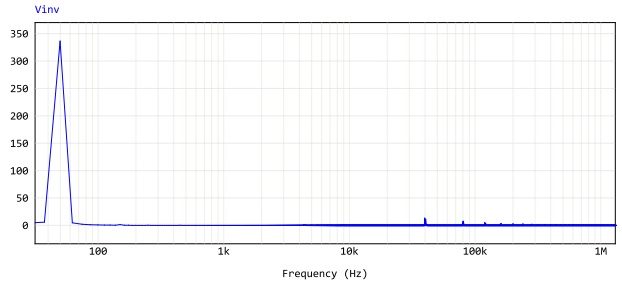

FIGURE 22. The harmonic spectra of the inverter voltage before filtration.

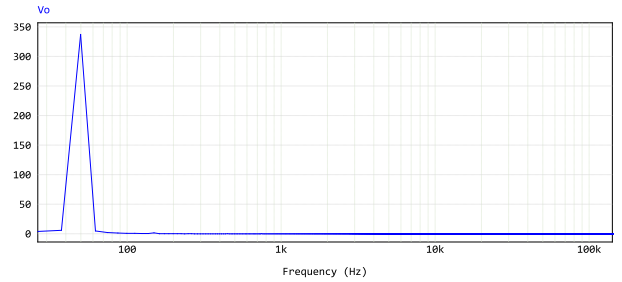

FIGURE 23. Harmonic spectra of the output voltage.

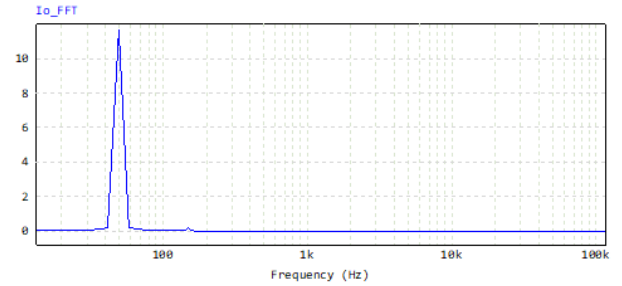

FIGURE 24. Harmonic spectra of the output current.

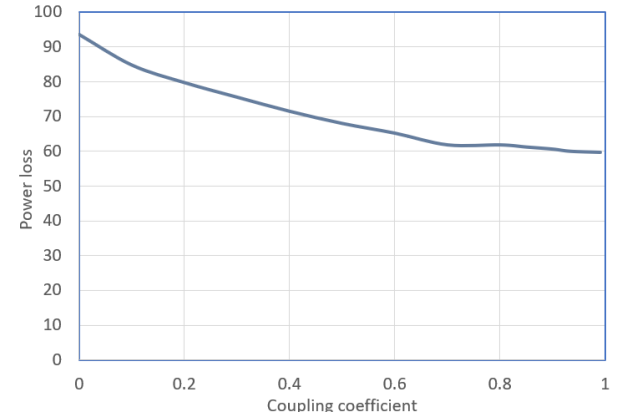

FIGURE 25. Power loss of the coupled inductor boost converter at different coupling coefficients.

A PEM.IGBT.03.A.0650.40 IGBT module that contains 6 IGBTs rating 650V, 40A. One IGBT is used for the boost switch S_b and four IGBTs are used as the inverter switches $S_1 - S_4$ and the body diode of the last one is utilized as

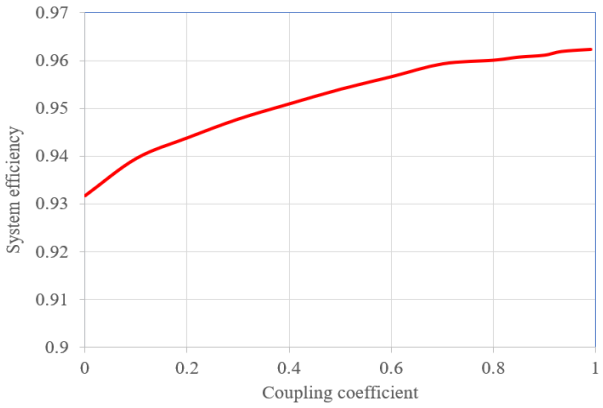

FIGURE 26. System conversion efficiency at different coupling coefficients.

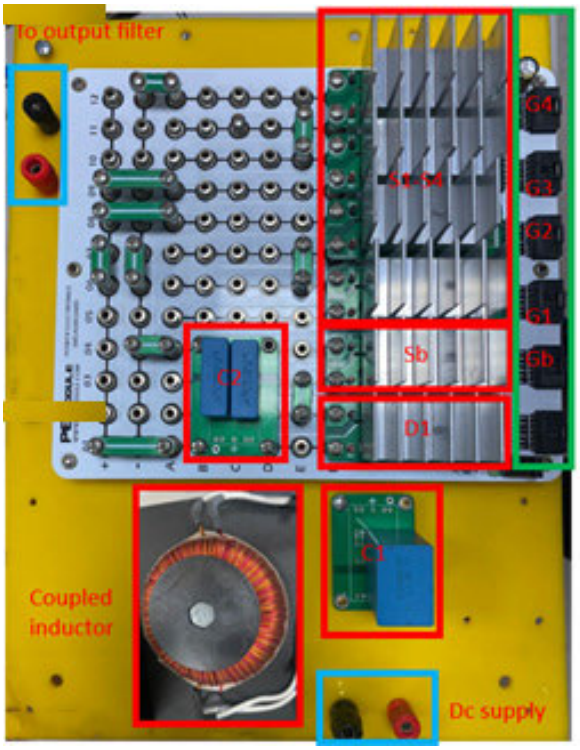

FIGURE 27. Appearance of the experimental setup.

the boost converter diode D_1. The Agilent DS07104A digital storage oscilloscope was used to record the current and voltage waveforms. Fig. 27 shows the total appearance of the hardware setup that was used in the lab. The experimental results are described and discussed in the following:

Fig. 28 demonstrates the gating signals from the control circuit shown in Fig. 6 for the boost switch S_b and the inverter switches $S_1 - S_4$, that perform the time-sharing operation described in Fig. 5 and simulated in Fig. 16. The experimental waveforms of the voltage and current of the boost inductor switch at input voltage of 160V are shown in Fig. 29. It can be noticed that the voltage and current waveforms of the boost switch coincide well with the intermediate modulated voltage

TABLE 4. Experimental prototype parameters.

Parameter	Symbol	Value
Rated power	P_o	2 kW
DC input voltage	V_i	160 V
Output voltage	V_o	220 V
Coupled inductor	L_p	2 mH
	L_s	2 mH
	K	0.93
Filter inductor	L_o	5 mH
Filter capacitor	C_o	10 uF
Switching frequency	f_s	40 kHz
Semiconductor devices	SW_c	PEM.IGBT.03.A.0650.4 0
	$S_1 - S_4$	
	D_1	

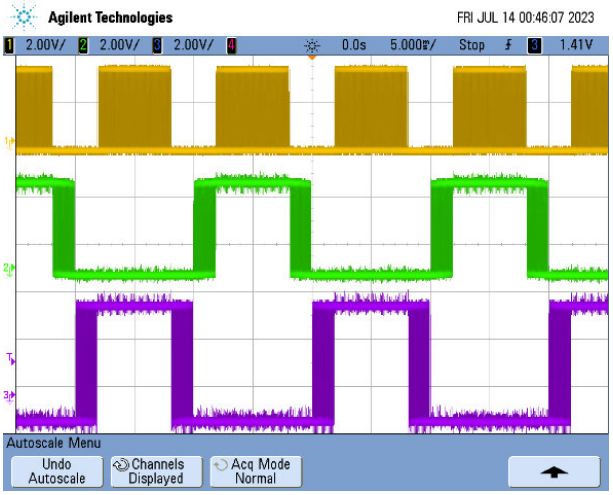

FIGURE 28. Gating signals, boost switch S_b (upper), inverter switches S_1 (middle) and S_3, (lower).

given in Fig. 19. From Fig. 29, it can be observed that the voltage spikes are almost negligible while the current spikes are about 1.25 of the peak modulated current.

Fig. 30 shows the experimental absolute quazi-sinewave modulated voltage waveform at the intermediate bus and the DC input voltage. This result is consistent with the simulated waveform of intermediate modulated voltage illustrated in Fig. 19. Experimental waveforms of intermediate modulated voltage and coupled inductor secondary winding current waveforms are shown in Fig. 31 that match the simulation results illustrated in Fig. 20. Fig. 32. depicts the DC input voltage, intermediate modulated voltage, and inverter output voltage waveforms. Intermediate modulated voltage, inverter output voltage, and the output voltage waveforms are displayed in Fig. 33. A high-quality sinusoidal output voltage and current waveforms are given in Fig. 34. Fig. 35 shows the relevant harmonic spectra of output current measured by FLUKE 43B Power Quality Analyzer. It can be noticed that a high-quality sinusoidal output current is realized with a total harmonic distortion of 1.1%.

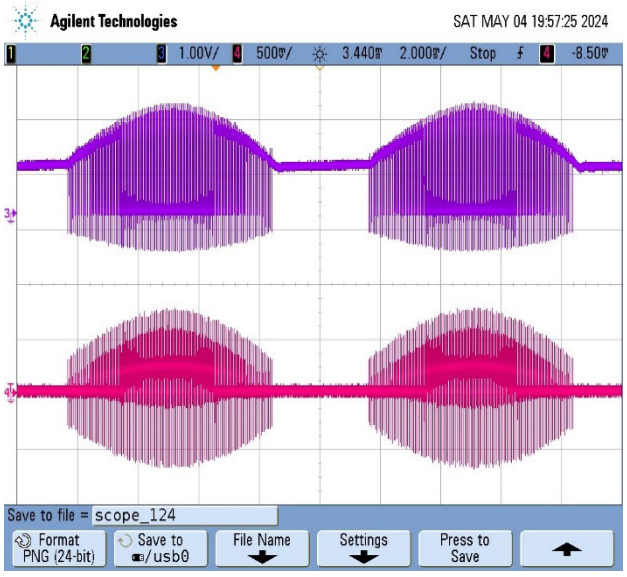

FIGURE 29. Voltage and current waveforms of boost inductor switch at input voltage of 160V.

FIGURE 30. Input voltage and intermediate modulated voltage.

VI. PERFORMANCE COMPARISON

A performance comparison between the proposed CIBB, two-stage, and conventional time-sharing microinverters are examined with the specifications given in Table 5. It can be noticed that the coupled inductor sizing requirement is significantly reduced for the proposed microinverter due to the ripple reduction advantage discussed in equations (21) to (24). Detailed power losses analysis is realized for these three microinverters and is demonstrated in Figs 36-38. Fig. 36 explains detailed power losses breakout out of the three microinverters described in Table 5 at an input voltage of 80V. It can be noticed that inductor power loss is considerably decreased in the proposed microinverter due to reduced inductor sizing requirement. In addition, the switching losses

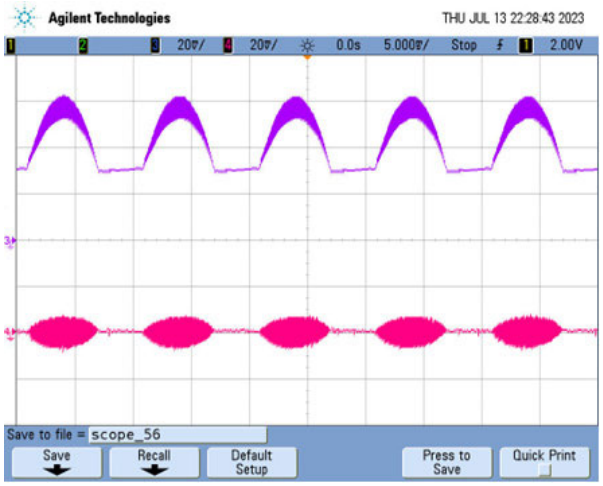

FIGURE 31. Experimental waveforms of intermediate modulated voltage and coupled inductor secondary winding current.

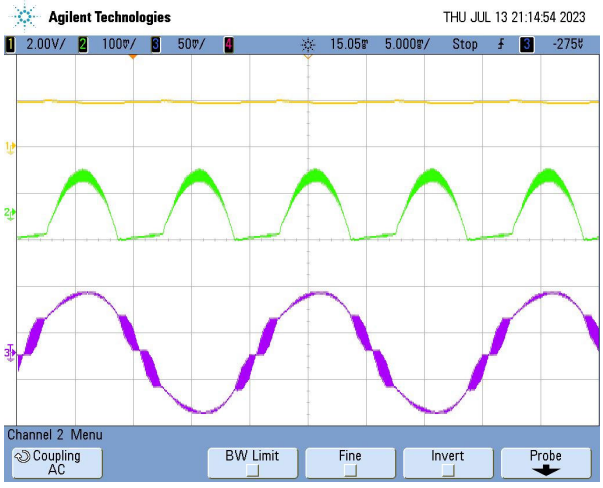

FIGURE 32. DC input voltage, intermediate modulated voltage and inverter output voltage waveforms.

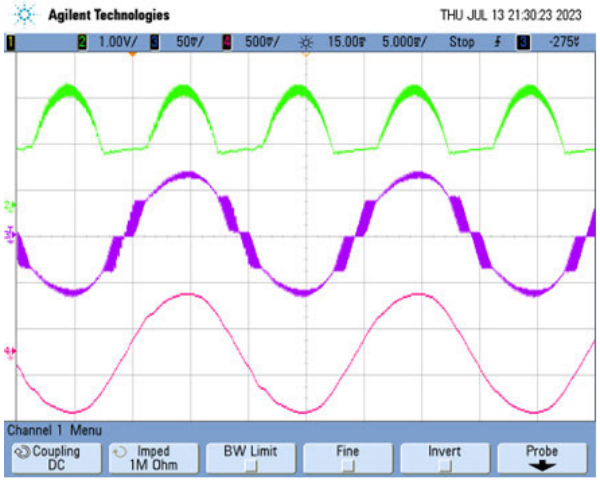

FIGURE 33. Intermediate modulated voltage, inverter output voltage, and the output voltage waveforms.

are significantly reduced due to utilization of the efficient dual mode time sharing operation principle.

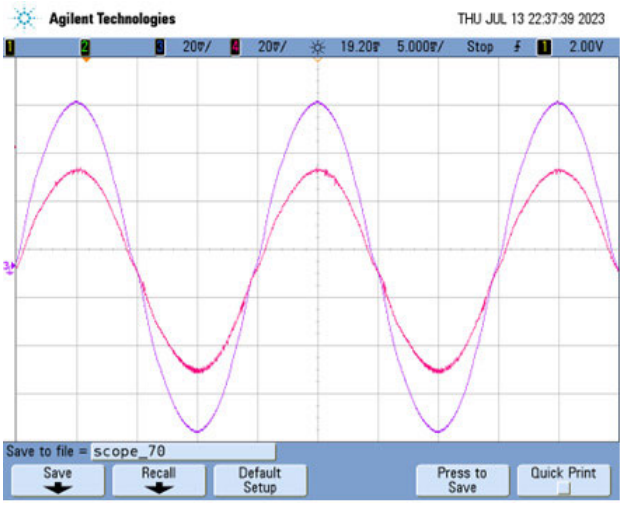

FIGURE 34. Experimental output voltage and current waveforms.

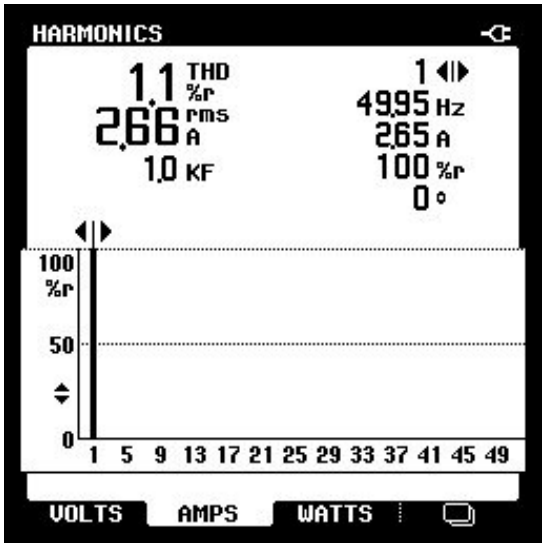

FIGURE 35. Total harmonic distortion of the output current.

TABLE 5. Comparison constants and circuit parameters.

Parameter	Symbol	Value		
		Conventional two Stage Micro inverter (Fig 3a)	Dual mode time sharing Microinverter (Fig. 3b)	Proposed CIBB Microinverter (Fig. 5)
Rated power	P_o	2.0 kW	2.0 kW	2.0 kW
Input voltage	V_i	80 V	80 V	80 V
Output voltage	V_o	240 V	240 V	240 V
Boost inductor	L_b	1 mH	1 mH	-
	L_p	-	-	150 uH
	L_s			150 uH
	K			0.93
Series capacitor	C_s	-	10 uF	10 uF
Intermediate capacitor	C_b	2200 uF	2.2 uF	2.2 uF
Filter capacitor	C_o	10 uF	10 uF	10 uF
Filter Inductor	L_o	2 mH	2 mH	2 mH
Switching frequency	f_s	40 kHz	40 kHz	40 kHz
Semiconductor devices	S_b, S_{1-4}	PEM.IGBT.03.A.0650.40 Module		
Efficiency	η	88%	93%	95%

Figs. 37 and 38 show the comparison of the power conversion efficiency of the three microinverters for different

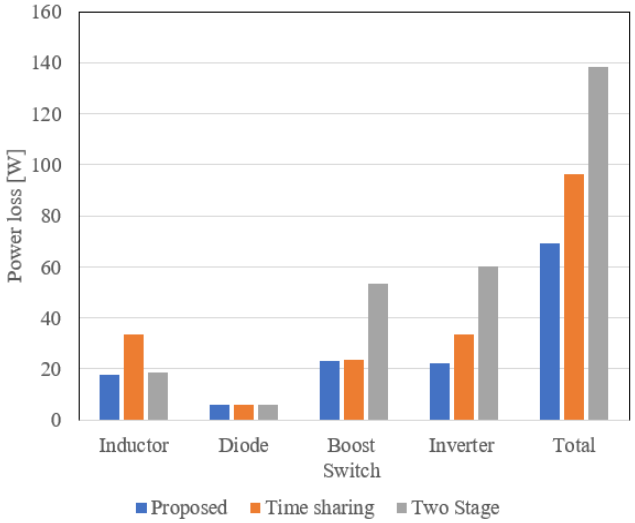

FIGURE 36. Comparison of power loss analysis.

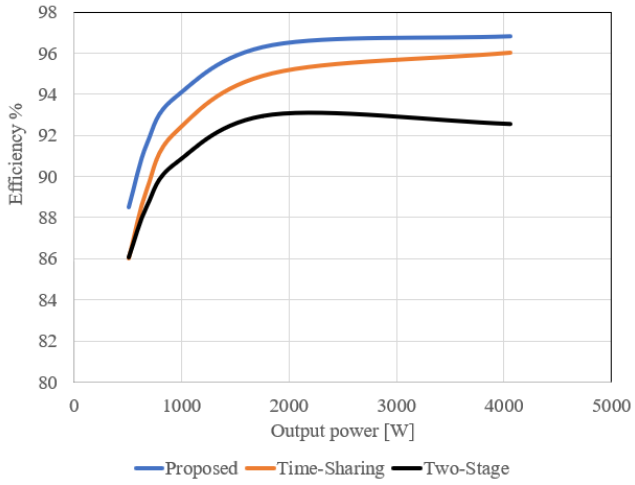

FIGURE 37. Comparison of power conversion efficiency at input voltage of 160V.

loading conditions at different input voltages of 160V and 80V, respectively. At input voltage of 160V, the proposed CIBB microinverter has a higher efficiency compared to the two-stage and conventional time-sharing microinverters, where it reaches its maximum value of 97% at the rated loading conditions of 2kW as shown in Fig. 27. Similarly, Fig. 38 depicts the power conversion efficiency in case of 80V input voltage where the proposed topology maintains the premier superior efficiency of 95% compared to the other microinverters. Furthermore, more efficiency improvement can be achieved via zero voltage switching (ZVS) scheme of the proposed CIBB by adding a soft switching cell to the boost switch S_b as described in [32].

The coupled inductors transfer energy from one winding to the other through the common core. They most are magnetically shielded for low electromagnetic interference (EMI) [46]. In fact, that the close coupling between the windings ($k > 0.9$) as suggested in this work results in low leakage inductance and generally provides more efficient energy

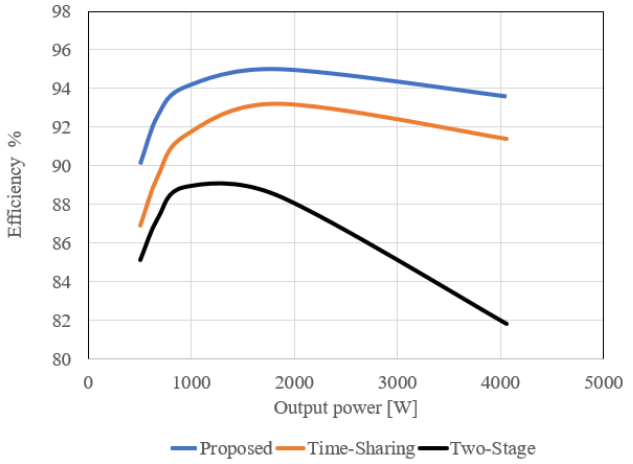

FIGURE 38. Comparison of power conversion efficiency at input voltage of 80V.

transfer and widest usable frequency bandwidth. In [47], details of EMI sources and mitigation techniques used in modern power electronics converters. EMI mitigation strategy for this CIBB microinverter is the usage of increased shielding to mitigate radiation.

VII. CONCLUSION

A coupled inductor-based boost microinverter is proposed in this study to enhance microinverter performance for more renewable energy deployment. The new microinverter topology allows a major reduction in boost inductor sizing due to significant reduction of current ripple magnitude. The current ripple can be reduced to one half in case of matching coupled inductor primary and secondary windings compared to the typical boost converter. In another scenario, the current ripple can be fully eliminated in either of the coupled inductor windings when winding inductance equals to the mutual inductance. In addition, the proposed microinverter topology offers a notable enhancement in power conversion performance that reached 97% and 95% peak efficiencies in case of 160V and 80V input voltage, respectively. This improvement is achieved due to efficient dual mode time sharing operation along with reduced coupled inductor size and inherently less power losses. Since the DC bus voltage is controlled to follow an absolute since wave, consequently, the bulky multi millifarads electrolytic capacitor is eliminated and replaced with 2.2μ film capacitor. The new microinverter prototype is constructed and tested for a 2kW rated setup and the resulted waveforms matched the proposed concept. The prototype generated a high-quality sinusoidal output of 1.1% total harmonic distortion.

REFERENCES

[1] A. Çiçek and O. Erdinç, "Risk-averse optimal bidding strategy considering bi-level approach for a renewable energy portfolio manager including EV parking lots for imbalance mitigation," *Sustain. Energy, Grids Netw.*, vol. 28, Dec. 2021, Art. no. 100539, doi: 10.1016/j.segan.2021.100539.

[2] A. Çiçek and O. Erdinç, "Optimal bidding strategy considering bilevel approach and multistage process for a renewable energy portfolio manager managing RESs with ESS," *IEEE Syst. J.*, vol. 16, no. 4, pp. 6062–6073, Dec. 2022, doi: 10.1109/JSYST.2021.3131138.

[3] W.-J. Cha, Y.-W. Cho, J.-M. Kwon, and B.-H. Kwon, "Highly efficient microinverter with soft-switching step-up converter and Single-Switch-Modulation inverter," *IEEE Trans. Ind. Electron.*, vol. 62, no. 6, pp. 3516–3523, Jun. 2015, doi: 10.1109/TIE.2014.2366718.

[4] A. K. Bhattacharjee and I. Batarseh, "Sinusoidally modulated AC-link microinverter based on dual-active-bridge topology," *IEEE Trans. Ind. Appl.*, vol. 56, no. 1, pp. 422–435, Jan. 2020, doi: 10.1109/TIA.2019.2943119.

[5] O. Kwon, K.-S. Kim, and B.-H. Kwon, "Highly efficient single-stage DAB microinverter using a novel modulation strategy to minimize reactive power," *IEEE J. Emerg. Sel. Topics Power Electron.*, vol. 10, no. 1, pp. 544–552, Feb. 2022, doi: 10.1109/JESTPE.2021.3090097.

[6] R. Aliaga, J. Muñoz, M. Rivera, P. Wheeler, J. Rohten, and A. Trentin, "A single phase hybrid multiport microinverter for photovoltaic energy controlled by exact linearization," *IEEE Access*, vol. 11, pp. 50075–50089, 2023, doi: 10.1109/ACCESS.2023.3278099.

[7] MarketWatch. (2026). *Micro-Inverter Market Size, Share, Report, Analysis, Trends & Forecast To 2026*. Accessed: Nov. 3, 2019. [Online]. Available: https://www.marketwatch.com/press-release/micro-inverter-market-size-share-report-analysis-trends-forecast-to-2026-2019-01-31

[8] K. Alluhaybi, I. Batarseh, and H. Hu, "Comprehensive review and comparison of single-phase grid-tied photovoltaic microinverters," *IEEE J. Emerg. Sel. Topics Power Electron.*, vol. 8, no. 2, pp. 1310–1329, Jun. 2020, doi: 10.1109/JESTPE.2019.2900413.

[9] S. Pal and S. Chattopadhyay, "Autonomous control schemes for grid-interfaced series-connected low-voltage isolated PV microinverter," in *Proc. IEEE Appl. Power Electron. Conf. Expo. (APEC)*, Orlando, FL, USA, Mar. 2023, pp. 1475–1482, doi: 10.1109/APEC43580.2023.10131383.

[10] H. Wu, X. Tang, J. Zhao, and Y. Xing, "An isolated bidirectional microinverter based on voltage-in-phase PWM-controlled resonant converter," *IEEE Trans. Power Electron.*, vol. 36, no. 1, pp. 562–570, Jan. 2021, doi: 10.1109/TPEL.2020.2997981.

[11] N. Kummari, S. Chakraborty, and S. Chattopadhyay, "An isolated high-frequency link microinverter operated with secondary-side modulation for efficiency improvement," *IEEE Trans. Power Electron.*, vol. 33, no. 3, pp. 2187–2200, Mar. 2018, doi: 10.1109/TPEL.2017.2699945.

[12] S. Chakraborty and S. Chattopadhyay, "A dual-active-bridge-based fully ZVS HF-isolated inverter with low decoupling capacitance," *IEEE Trans. Power Electron.*, vol. 35, no. 3, pp. 2615–2628, Mar. 2020, doi: 10.1109/TPEL.2019.2927596.

[13] D. Yang, H. Zhang, C. Liu, Z. Pei, L. Lin, and X. Song, "Novel high-frequency isolated cascade PV inverter topology based on multi-bus DC collection," *IEEE J. Emerg. Sel. Topics Power Electron.*, vol. 9, no. 2, pp. 2122–2135, Apr. 2021, doi: 10.1109/JESTPE.2020.2968914.

[14] O. Lopez-Santos, C. A. Jacanamejoy-Jamioy, D. F. Salazar-D'Antonio, J. R. Corredor-Ramírez, G. Garcia, and L. Martinez-Salamero, "A single-phase transformer-based cascaded asymmetric multilevel inverter with balanced power distribution," *IEEE Access*, vol. 7, pp. 98182–98196, 2019, doi: 10.1109/ACCESS.2019.2930230.

[15] T. Zhao, V. Bhavaraju, P. Nirantare, and J. Xu, "Evaluation of commercial scale transformerless solar inverter technology," in *Proc. IEEE Energy Convers. Congr. Expo. (ECCE)*, Sep. 2015, pp. 5342–5348, doi: 10.1109/ECCE.2015.7310411.

[16] D. Debnath and K. Chatterjee, "Two-stage solar photovoltaic-based stand-alone scheme having battery as energy storage element for rural deployment," *IEEE Trans. Ind. Electron.*, vol. 62, no. 7, pp. 4148–4157, Jul. 2015, doi: 10.1109/TIE.2014.2379584.

[17] Z. Aleem, S. L. Winberg, H. F. Ahmed, and J.-W. Park, "Parallel operation of transformer-based improved Z-source inverter with high boost and interleaved control," *IEEE Trans. Ind. Informat.*, vol. 18, no. 4, pp. 2422–2433, Apr. 2022, doi: 10.1109/TII.2021.3098685.

[18] M. A. Anthony, P. Ling, and J. Meijer, "The safety and economic benefit of reduced power design densities permitted in the 2014 national electrical code," in *Proc. IEEE/IAS 50th Ind. Commercial Power Syst. Tech. Conf.*, May 2014, pp. 1–6, doi: 10.1109/ICPS.2014.6839169.

[19] X. Zhu, H. Wang, W. Zhang, H. Wang, X. Deng, and X. Yue, "A novel single-phase five-level transformer-less photovoltaic (PV) inverter," *CES Trans. Electr. Mach. Syst.*, vol. 4, no. 4, pp. 329–338, Dec. 2020, doi: 10.30941/CESTEMS.2020.00040.

[20] M. Rajeev and V. Agarwal, "Analysis and control of a novel transformer-less microinverter for PV-grid interface," *IEEE J. Photovolt.*, vol. 8, no. 4, pp. 1110–1118, Jul. 2018, doi: 10.1109/JPHOTOV.2018.2825298.

[21] J. Roy and R. Ayyanar, "GaN based transformer-less microinverter with coupled inductor interleaved boost and half bridge voltage swing inverter," in *Proc. IEEE Appl. Power Electron. Conf. Expo. (APEC)*, Mar. 2018, pp. 381–386, doi: 10.1109/APEC.2018.8341039.

[22] A. Jamatia, V. Gautam, and P. Sensarma, "Power decoupling for single-phase PV system using Cuk derived microinverter," *IEEE Trans. Ind. Appl.*, vol. 54, no. 4, pp. 3586–3595, 2018, doi: 10.1109/TIA.2018.2812140.

[23] S. J. Castillo, R. S. Balog, and P. Enjeti, "Predicting capacitor reliability in a module-integrated photovoltaic inverter using stress factors from an environmental usage model," in *Proc. North Amer. Power Symp.*, Sep. 2010, pp. 1–6, doi: 10.1109/NAPS.2010.5618955.

[24] J. Jia, Q. Li, Y. Wang, Y. T. Cham, and M. Han, "Modeling and dynamic characteristic simulation of proton exchange membrane fuel cell," *IEEE Trans. Control Syst. Technol*, vol. 24, no. 16, pp. 283–291, Mar. 2009.

[25] M. Ceraolo, C. Miulli, and A. Pozio, "Modelling static and dynamic behaviour of proton exchange membrane fuel cells on the basis of electro-chemical description," *J. Power Sources*, vol. 113, no. 1, pp. 131–144, Jan. 2003.

[26] J. C. Amphlett, R. F. Mann, B. A. Peppley, P. R. Roberge, and A. Rodrigues, "A model predicting transient responses of proton exchange membrane fuel cells," *J. Power Sources*, vol. 61, nos. 1–2, pp. 183–188, Jul. 1996.

[27] R. J. Talj, D. Hissel, R. Ortega, M. Becherif, and M. Hilairet, "Experimental validation of a PEM fuel-cell reduced-order model and a moto-compressor higher order sliding-mode control," *IEEE Trans. Ind. Electron.*, vol. 57, no. 6, pp. 1906–1913, Jun. 2010.

[28] N. Ahmed, "Computational modeling and polarization characteristics of proton exchange membrane fuel cell with evaluation of its interface systems," *EPE J.*, vol. 18, no. 1, pp. 32–41, Mar. 2008.

[29] F. Edwin, W. Xiao, and V. Khadkikar, "Topology review of single phase grid-connected module integrated converters for PV applications," in *Proc. IECON 38th Annu. Conf. IEEE Ind. Electron. Soc.*, Montreal, QC, Canada, Oct. 2012, pp. 821–827, doi: 10.1109/IECON.2012.6388645.

[30] W. Xiao, *Photovoltaic Power System Modeling, Design, and Control*. Hoboken, NJ, USA: Wiley, 2017.

[31] F. F. Edwin, W. Xiao, and V. Khadkikar, "Dynamic modeling and control of interleaved flyback module-integrated converter for PV power applications," *IEEE Trans. Ind. Electron.*, vol. 61, no. 3, pp. 1377–1388, Mar. 2014, doi: 10.1109/TIE.2013.2258309.

[32] N. A. Ahmed, H. W. Lee, and M. Nakaoka, "Dual-mode time-sharing sinewave-modulation soft switching boost full-bridge one-stage power conditioner without electrolytic capacitor DC link," *IEEE Trans. Ind. Appl.*, vol. 43, no. 3, pp. 805–813, May 2007, doi: 10.1109/TIA.2007.895803.

[33] J. Madouh, N. A. Ahmed, and A. M. Al-Kandari, "Advanced power conditioner using sinewave modulated buck–boost converter cascaded polarity changing inverter," *Int. J. Electr. Power Energy Syst.*, vol. 43, no. 1, pp. 280–289, Dec. 2012, doi: 10.1016/j.ijepes.2012.05.002.

[34] N. A. Ahmed, B. Saha, M. Miyatake, H. W. Lee, and M. Nakaoka, "Advanced single-stage soft switching PWM power conditioner with coupled inductor PWM boost chopper cascaded PWM inverter and time-sharing sinusoidal follow-up control scheme," in *Proc. 37th IEEE Power Electron. Spec. Conf.*, Jun. 2006, pp. 2017–2023.

[35] W. Wu and T. Tang, "Dual-mode time-sharing cascaded sinusoidal inverter," *IEEE Trans. Energy Convers.*, vol. 22, no. 3, pp. 795–797, Sep. 2007, doi: 10.1109/TEC.2007.902672.

[36] F. M. Alhuwaishel and N. A. Ahmed, "Single stage transformerless microinverter with time sharing operation for PEM fuel cell applications," in *Proc. IEEE Conf. Power Electron. Renew. Energy (CPERE)*, Luxor, Egypt, Feb. 2023, pp. 1–6, doi: 10.1109/CPERE56564.2023.10119583.

[37] S. Sakhavati and E. Babaei, "Coupled inductor based boost DC/DC converter," in *Proc. 7th Power Electron. Drive Syst. Technol. Conf. (PEDSTC)*, Tehran, Iran, Feb. 2016, pp. 191–196, doi: 10.1109/PEDSTC.2016.7556860.

[38] A. K. Paul, B. S. Ram, and S. V. Kulkarni, "Review of coupled inductors in power electronics: From concept to practice," *e-Prime Adv. Electr. Eng., Electron. Energy*, vol. 8, Jun. 2024, Art. no. 100501, doi: 10.1016/j.prime.2024.100501.

[39] J.-P. Lee, H. Cha, D. Shin, K.-J. Lee, D.-W. Yoo, and J.-Y. Yoo, "Analysis and design of coupled inductors for two-phase interleaved DC–DC converters," *J. Power Electron.*, vol. 13, no. 3, pp. 339–348, May 2013.

[40] G. T. Götz, A. Stippich, A. H. Wienhausen, and R. W. De Doncker, "Design of coupled inductor for two-phase synchronous boost converters in automotive applications," in *Proc. IEEE Appl. Power Electron. Conf. Expo. (APEC)*, New Orleans, LA, USA, Mar. 2020, pp. 2658–2665, doi: 10.1109/APEC39645.2020.9124143.

[41] J. L. Kotny, X. Margueron, and N. Idir, "Coupling inductor models for EMI filters," in *Proc. 35th Annu. Conf. IEEE Ind. Electron.*, Porto, Portugal, Nov. 2009, pp. 4092–4097, doi: 10.1109/IECON.2009.5415099.

[42] R. Mottet, M. Almanza, A. Boegli, and Y. Perriard, "Critical parasitic elements of coupled inductors for ultra-high voltage flyback converters used to drive capacitive actuators," in *Proc. 22nd Int. Conf. Electr. Mach. Syst. (ICEMS)*, Harbin, China, Aug. 2019, pp. 1–5, doi: 10.1109/ICEMS.2019.8921772.

[43] W. Martinez, C. Cortes, M. Yamamoto, and J. Imaoka, "Effect of inductor parasitic resistances on the voltage gain of high step-up DC–DC converters for electric vehicle applications," *IET Power Electron.*, vol. 11, pp. 1628–1639, Jun. 2018, doi: 10.1049/iet-pel.2017.0361.

[44] *IEEE Recommended Practice and Requirements for Harmonic Control in Electric Power Systems*, Standard 519-2014 (Revision IEEE Std 519-1992), Jun. 2014, pp. 1–29, doi: 10.1109/IEEESTD.2014.6826459.

[45] A. Erenoğlu, A. Çiçek, O. Arıkan, O. Erdinç, and J. P. S. Catalão, "A new approach for grid-connected hybrid renewable energy system sizing considering harmonic contents of smart home appliances," *Appl. Sci.*, vol. 9, no. 18, p. 3941, Sep. 2019, doi: 10.3390/app9183941.

[46] (2024). *A Guide To Coupled Inductors, Coilcraft*. Accessed: Apr. 8, 2024. [Online]. Available: https://www.coilcraft.com/en-us/edu/series/a-guide-to-coupled-inductors/

[47] L. Yuan, J. Zhang, Z. Liang, M. Hu, G. Chen, and W. Lu, "EMI challenges in modern power electronic-based converters: Recent advances and mitigation techniques," *Frontiers Electron.*, vol. 4, Nov. 2023, Art. no. 1274258.

FAHAD M. ALHUWAISHEL (Member, IEEE) received the B.E. degree in electrical engineering from Kuwait University, in 2010, and the M.Sc. and Ph.D. degrees in electrical engineering from Texas A&M University, in 2015 and 2021, respectively. In 2010, he joined an internship program with Hyundai Engineering, Seoul, South Korea. He joined an internship program with the Wireline Department, Shlumberger, Kuwait. In 2011, he joined the Technology Improvement Department, EQUATE Petrochemical Company, as an Analyzer Engineer, Kuwait. In 2015, he joined the College of Technological Studies, Public Authority for Applied Education and Training, Kuwait, where he is currently an Assistant Professor. He is the holder of three U.S. patents. He has several publications within IEEE conferences/journals. He also served as a Reviewer for IAS, IEEE JOURNAL OF EMERGING AND SELECTED TOPICS IN POWER ELECTRONICS, and IEEE TRANSACTIONS ON TRANSPORTATION ELECTRIFICATION. His research interests include advanced power electronics, smart cities, renewable energy systems, high voltage dc transmission (HVDC), battery storage systems, unmanned aircraft systems (UAVs), electric vehicles (EVs), and adjustable speed drives (ASD). He was honored to receive the prestigious Recognition Award by the Amir of Kuwait, in 2010. He was a recipient of the Golden Award from the Genève International Invention Expedition, in 2010. He is a nationwide referee in the state of Kuwait for inventions category.

NABIL A. AHMED (Senior Member, IEEE) received the B.Sc. and M.Sc. degrees in electrical engineering from the Electrical and Electronics Engineering Department, Assiut University, Egypt, in 1989 and 1994, respectively, and the Ph.D. degree in electrical engineering from the University of Toyama, Japan, in 2000. Since 1989, he has been with Assiut University, where he has been a Professor, since 2011. From October 2004 to April 2005, he was a Postdoctoral Fellow with the Electrical Engineering Saving Research Center, Kyungnam University, South Korea. From July 2005 to September 2006, he was a JSPS Postdoctoral Fellow with Sophia University, Japan. He is currently an Associate Professor with the Electrical Engineering Department, College of Technological Studies, The Public Authority for Applied Education and Training, Kuwait; on leave from Assiut University. His research interests include power electronics applications, variable speed drives, soft switching converters, and renewable energy systems and its integration to electric power grid. He is a Senior Member of the IEEE Industrial Electronics Society. He was a recipient of Egypt State Encouraging of Research Prize 2005, Japan Monbusho Scholarship 1996–2000, JSPS Fellowship 2005–2007, the Best Paper Award from ICEMS 2005 and IATC 2006 conferences, and the Best Presentation Award from ICEMS 2004 Conference. He has been listed in Marque's Who is Who in the World, since 2009.